27. D. L. Swenson *et al.*, *Vaccine* **23**, 3033–3042 (2005).
28. K. L. Warfield *et al.*, *J. Immunol.* **175**, 1184–1191 (2005).
29. E. S. Kempner, *J. Pharm. Sci.* **90**, 1637–1646 (2001).

ACKNOWLEDGMENTS

We thank E. Ollmann-Saphire (Scripps Research Institute, La Jolla, CA) for purified EBOV NP. We also thank S. Watson for editing the manuscript, T. Armbrust for excellent technical assistance, and staff of the Rocky Mountain Veterinary Branch for assistance with animal work. Y.K. and G.N. are inventors on a patent (held by the University of Wisconsin Alumni Research Foundation) for EBOV reverse genetics; therefore, a Material Transfer Agreement (MTA) is required to obtain this system. Funding for this research was provided by the Region V "Great Lakes" Regional Center of Excellence (GLRCE; U54 AI 57153) and by Health and Labour Sciences Research Grants, Japan. The study was partially funded by the Intramural Research Program of the National Institute of Allergy and Infectious Diseases, NIH. Raw data can be found at https://docs.google.com/spreadsheets/d/1dBgzt5_z4rp-qOuxXcl_FbUz8wNqMvHy6kVP_tpWOMY/edit?usp=sharing.

SUPPLEMENTARY MATERIALS

www.sciencemag.org/content/348/6233/439/suppl/DC1
Materials and Methods
Tables S1 to S3
Figs. S1 and S2

14 December 2014; accepted 13 March 2015
Published online 26 March 2015;
10.1126/science.aaa4919

GENOME EDITING

The mutagenic chain reaction: A method for converting heterozygous to homozygous mutations

Valentino M. Gantz* and Ethan Bier*

An organism with a single recessive loss-of-function allele will typically have a wild-type phenotype, whereas individuals homozygous for two copies of the allele will display a mutant phenotype. We have developed a method called the mutagenic chain reaction (MCR), which is based on the CRISPR/Cas9 genome-editing system for generating autocatalytic mutations, to produce homozygous loss-of-function mutations. In *Drosophila*, we found that MCR mutations efficiently spread from their chromosome of origin to the homologous chromosome, thereby converting heterozygous mutations to homozygosity in the vast majority of somatic and germline cells. MCR technology should have broad applications in diverse organisms.

It is often desirable to generate recessive loss-of-function mutations in emergent model organisms; however, identifying such mutations in the heterozygous condition is challenging. Taking advantage of the CRISPR/Cas9 genome-editing method (*1*, *2*), we have developed a strategy to convert a *Drosophila* heterozygous recessive mutation into a homozygous condition manifesting a mutant phenotype. We reasoned that autocatalytic insertional mutants could be generated with a construct having three components: (i) A *Cas9* gene (expressed in both somatic and germline cells), (ii) a guide RNA (gRNA) targeted to a genomic sequence of interest, and (iii) homology arms flanking the Cas9-gRNA cassettes that match the two genomic sequences immediately adjacent to either side of the target cut site (Fig. 1A). In such a tripartite construct, Cas9 should cleave the genomic target at the site determined by the gRNA (Fig. 1A) and then insert the Cas9-gRNA cassette into that locus via homology-directed repair (HDR) (Fig. 1, B and C). Cas9 and the gRNA produced from the insertion allele should then cleave the opposing allele (Fig. 1D), followed by HDR-driven propagation of the Cas9-gRNA cassette to the companion chromosome (Fig. 1, E and F). We refer to this trans-acting mutagenesis scheme as a mutagenic chain reaction (MCR).

We expected that autocatalytic allelic conversion by MCR should be very efficient in both somatic and germline precursor cells, given the high frequency and specificity of mutagenesis (*3*)

Section of Cell and Developmental Biology, University of California, San Diego, La Jolla, CA 92095, USA.
*Corresponding author. E-mail: vgantz@ucsd.edu (V.M.G.); ebier@ucsd.edu (E.B.)

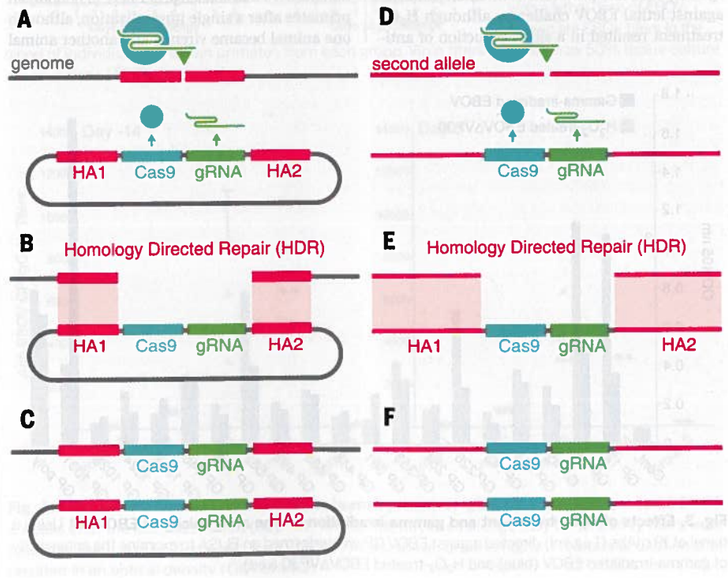

Fig. 1. Scheme outlining the mutagenic chain reaction (MCR). (**A** to **C**) A plasmid consisting of a core cassette carrying a *Cas9* transgene, a gRNA targeting a genomic sequence of interest, and flanking homology arms corresponding to genomic sequences abutting the target cleavage site (A) inserts the core Cas9-gRNA cassette into the targeted locus via HDR [(B) and (C)]. (**D** to **F**) In turn, the inserted cassette expresses both Cas9 and the gRNA, leading to cleavage (D) and HDR-mediated insertion of the cassette into the second allele, thereby rendering the mutation homozygous [(E) and (F)]. HA1 and HA2 denote the two homology arms that directly flank the gRNA-directed cut site.

and efficacy of homology-based integration (*4*) mediated by separate genome-encoded *Cas9* and gRNA genes observed in previous studies. We tested this prediction in *D. melanogaster* with the use of a characterized efficient target sequence (*y1*) (*5*) in the X-linked *yellow* (*y*) locus as the gRNA target and a *vasa-Cas9* transgene as a source of Cas9 (Fig. 2C) because it is expressed in both germline and somatic cells (*4*). As the defining element of our MCR scheme, we also included two homology arms, ~1 kb each, flanking the central elements (Fig. 2C) that precisely abut the gRNA-directed cut site. Wild-type (*y+*) embryos were injected with the *y*-MCR element (see supplementary materials), and emerging F_0 flies were crossed to a *y+* stock. According to Mendelian inheritance, all F_1 female progeny of such a cross should have a *y+* phenotype (i.e., F_1 females inherit a *y+* allele from their wild-type parent).

From two independent F_0 male (♂) × *y+* female (♀) crosses and 7 F_0♀ × *y+*♂ crosses, we recovered *y*– F_1♀ progeny, which should not happen according to Mendelian inheritance of a recessive allele. Six such y^{MCR} F_1♀ were crossed individually to *y+*♂, resulting in 95 to 100% (average = 97%) of their F_2 progeny exhibiting a full-bodied *y*– phenotype (Fig. 2, E and G, and table S1), in contrast to the expected rate of 50% (i.e., only in males). We similarly tested MCR transmission via the germline in two *y*– F_1♂ recovered from an F_0♀ cross that also yielded *y*– female siblings. These *y*– F_1♂ were considered candidates for carrying the *y*-MCR construct and were crossed to *y+* females. All but one of their F_2 female progeny had a full-bodied *y*– phenotype (Fig. 2, E and F). Occasionally among y^{MCR} F_2♀ we also recovered mosaics (~4%) with a few small *y+* patches as well as a lone example of a 50% chimeric female (Fig. 2H), and in two instances, we recovered *y+* male progeny from a y^{MCR} F_1♀ mother (Fig. 2E and table S1). These infrequent examples of imperfect *y*-MCR transmission indicate that although HDR is highly efficient at this locus in both somatic and germline lineages, the target occasionally evades conversion.

Polymerase chain reaction (PCR) analysis of the *y* locus in individual *y*– F_1 progeny confirmed the precise gRNA- and HDR-directed genomic insertion of the *y*-MCR construct in all flies giving rise to *y*– female F_2 progeny (Fig. 2D). Males carried only this single allele, as expected, whereas females in addition possessed a band corresponding to the size of the wild-type *y* locus (Fig. 2D, lane 4), which varied in intensity between individuals, indicating that females were mosaic for MCR conversion. The left and right *y*-MCR PCR junction fragments were sequenced from *y*– F_1 progeny from five independent F_0 parents. All had the precise expected HDR-driven insertion of the *y*-MCR element into the chromosomal *y* locus. In addition, sequence analysis of a rare nonconverted *y+* allele recovered in a male offspring from a y^{MCR} F_1♀ (Fig. 2E) revealed a single-nucleotide change at the gRNA cut site (resulting in a T→I substitution), which most likely resulted from nonhomologous end-joining repair, as well as an in-frame insertion-deletion (indel) in a *y+*♀ sibling of this male (fig. S1 and table S1). The high recovery rate of full-bodied *y*– F_1 and F_2 female progeny from single parents containing a y^{MCR} allele detectable by PCR indicates that the conversion process is remarkably efficient in both somatic and germline lineages. Phenotypic evidence of mosaicism in a small percentage of MCR-carrying females and the presence of *y* locus–derived PCR products of wild-type size in all tested *y*– F_1 females suggest that females may all be mosaic to varying degrees. In summary, both genetic and molecular data reveal that the *y*-MCR element efficiently drives allelic conversion in somatic and germline lineages.

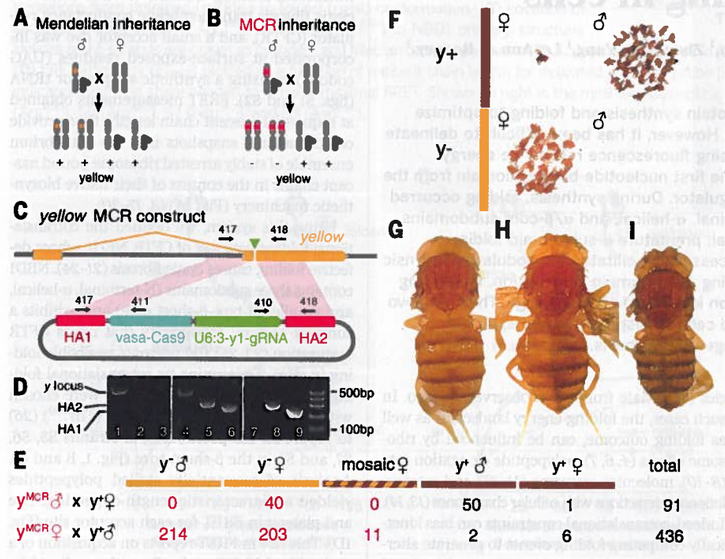

Fig. 2. Experimental demonstration of MCR in *Drosophila*. (**A**) Mendelian male inheritance of an X-linked trait. (**B**) Theoretical MCR-based inheritance results in the initially heterozygous allele converting the second allele, thereby generating homozygous female progeny. (**C**) Diagram of *y*-MCR construct. Two *y* locus homology arms flanking the *vasa-Cas9* and *y*-gRNA transgenes are indicated, as are the locations of the PCR primers used for analysis of the genomic insertion site (see supplementary materials). (**D**) PCR analysis of a *y+* MCR-derived F_2♂ (lanes 1 to 3; see fig. S1 for sequence), y^{MCR} F_1♀ (lanes 4 to 6), and y^{MCR} F_1♂ (lanes 7 to 9) showing junctional bands corresponding to *y*-MCR insertion into the chromosomal *y* locus (lanes 2, 3, 5, 6, 8, and 9) and the presence (lanes 1 and 4) or absence (lane 7) of a PCR band derived from the *y* locus. Although the y^{MCR} F_1♂ (carrying a single X chromosome) displays only MCR-derived PCR products (lanes 8 and 9), y^{MCR} F_1♀s generate both MCR and noninsertional amplification products. (**E**) Summary of F_2 progeny obtained from crosses described in table S1. (**F**) Low-magnification view of F_2 progeny flies from an y^{MCR} ♂× *y+*♀ cross. Nearly all female progeny display a *y*– phenotype. (**G**) High-magnification view of a full-bodied y^{MCR} F_1♀. (**H**) A rare 50% left-right mosaic female. (**I**) A *y+* control fly.

In addition to these positive applications of MCR technology, we are also keenly aware of the substantial risks associated with this highly invasive method. Failure to take stringent precautions could lead to the unintentional release of MCR organisms into the environment. The supplementary material includes a stringent, institutionally approved barrier containment protocol that we developed and are currently adhering to for MCR experiments. Since this study was

submitted for publication, a preprint has been posted on the bioRxiv web server showing that a split Cas9-gRNA gene drive system efficiently biases inheritance in yeast (*6*). The split system was used to avoid accidental escape of the gene drives. The use of a similar strategy in future MCR organisms would reduce, but not eliminate, risks associated with accidental release. We therefore concur with others (*7, 8*) that a dialogue on this topic should become an immediate high-priority issue. Perhaps, by analogy to the famous Asilomar meeting of 1975 that assessed the risks of recombinant DNA technology, a similar conference could be convened to consider biosafety measures and institutional policies appropriate for limiting the risk of engaging in MCR research while affording workable opportunities for positive applications of this concept.

REFERENCES AND NOTES

1. F. Zhang, Y. Wen, X. Guo, *Hum. Mol. Genet.* **23**, R40–R46 (2014).
2. P. D. Hsu, E. S. Lander, F. Zhang, *Cell* **157**, 1262–1278 (2014).
3. F. Port, H. M. Chen, T. Lee, S. L. Bullock, *Proc. Natl. Acad. Sci. U.S.A.* **111**, E2967–E2976 (2014).
4. S. J. Gratz *et al.*, *Genetics* **196**, 961–971 (2014).
5. A. R. Bassett, C. Tibbit, C. P. Ponting, J. L. Liu, *Cell Rep.* **4**, 220–228 (2013).
6. J. E. DiCarlo, A. Chavez, S. L. Dietz, K. M. Esvelt, G. M. Church, http://biorxiv.org/content/early/2015/01/16/013896 (2015).
7. K. A. Oye *et al.*, *Science* **345**, 626–628 (2014).
8. K. M. Esvelt, A. L. Smidler, F. Catteruccia, G. M. Church, *eLife* 10.7554/eLife.03401 (2014).

ACKNOWLEDGMENTS

We thank M. Yanofsky, W. McGinnis, S. Wasserman, R. Kolodner, H. Bellen, and members of the Bier lab for helpful discussions and comments on the manuscript; M. Harrison, K. O'Connor-Giles, J. Wildonger, and S. Bullock for providing CRISPR/Cas9 reagents and information; and J. Vinetz and A. Lubar for granting us access to their BSL2 insectary. Supported by NIH grants R01 GM067247 and R56 NS029870 and by a generous gift from S. Sandell and M. Marshall. E.B. and V.M.G. are authors on a patent applied for by the University of California, San Diego (provisional patent application number 62075534) that relates to the mutagenic chain reaction. MCR fly stocks and DNA constructs are available from E.B. under a material transfer agreement from UCSD. This protocol for use and containment of our MCR stocks in a BSL2 barrier insectary also used for containment of malaria-infected mosquitos was reviewed and approved by the UCSD Institutional Biosafety Committee (BUA R461).

SUPPLEMENTARY MATERIALS

www.sciencemag.org/content/348/6233/442/suppl/DC1
Materials and Methods
Supplementary Text
Fig. S1
Table S1

31 December 2014; accepted 10 March 2015
Published online 19 March 2015;
10.1126/science.aaa5945

PROTEIN FOLDING

Translational tuning optimizes nascent protein folding in cells

Soo Jung Kim,[1] Jae Seok Yoon,[1] Hideki Shishido,[1] Zhongying Yang,[1] LeeAnn A. Rooney,[1] Jose M. Barral,[2,3] William R. Skach[1,4]*

In cells, biosynthetic machinery coordinates protein synthesis and folding to optimize efficiency and minimize off-pathway outcomes. However, it has been difficult to delineate experimentally the mechanisms responsible. Using fluorescence resonance energy transfer, we studied cotranslational folding of the first nucleotide-binding domain from the cystic fibrosis transmembrane conductance regulator. During synthesis, folding occurred discretely via sequential compaction of N-terminal, α-helical, and α/β-core subdomains. Moreover, the timing of these events was critical; premature α-subdomain folding prevented subsequent core formation. This process was facilitated by modulating intrinsic folding propensity in three distinct ways: delaying α-subdomain compaction, facilitating β-strand intercalation, and optimizing translation kinetics via codon usage. Thus, de novo folding is translationally tuned by an integrated cellular response that shapes the cotranslational folding landscape at critical stages of synthesis.

Most proteins must acquire a defined three-dimensional structure in order to function. Folding pathways that generate these structures have primarily been characterized by using model substrates that fold rapidly, spontaneously, and reversibly in vitro (*1*, *2*). In cells, however, protein folding is kinetically coupled to synthesis as the nascent polypeptide emerges from the ribosome. Whereas certain small proteins may remain unstructured during synthesis (*3*), many complex proteins exhibit length-dependent folding intermediates whose structural properties (*4*) and/or folding efficiencies (*5*) deviate from those observed in vitro. In such cases, the folding energy landscape, as well as folding outcome, can be influenced by ribosome effects (*4*, *6*, *7*), polypeptide elongation rate (*8*–*10*), molecular crowding (*11*, *12*), and cotranslational interactions with cellular chaperones (*13*, *14*). Indeed, cotranslational constraints can bias kinetically competing folding events to generate alternate stable structures with different functional properties (*8*, *15*, *16*). Despite improved computational methods, few principles have been established experimentally to explain how biosynthetic parameters influence specific folding events and outcome (*3*, *4*, *17*–*19*).

To address this issue, we used fluorescence resonance energy transfer (FRET) to examine structural transitions of ribosome-bound folding intermediates generated through in vitro translation of truncated RNA transcripts. This approach derives from the principle that during folding, certain residues distant in primary structure are brought into close proximity, increasing the FRET efficiency between donor and acceptor fluorophores that are cotranslationally incorporated into the nascent polypeptide (Fig. 1A) (*18*, *19*). Here, the donor fluorophore, cyan fluorescent protein (CFP), was fused to the N terminus of the first nucleotide-binding domain (NBD1) from the cystic fibrosis transmembrane conductance regulator (CFTR), and a small acceptor dye was incorporated at surface-exposed residues (UAG codons) by using a synthetic suppressor tRNA (figs. S1 and S2). FRET measurements obtained at sequential nascent chain lengths thus provide conformational snapshots into the equilibrium ensemble of stably arrested ribosome-bound nascent chains in the context of their native biosynthetic machinery (Fig. 1A) (*3*, *17*–*20*).

Using this system, we defined the cotranslational folding pathway of CFTR NBD1, whose defective folding causes cystic fibrosis (*21*–*24*). NBD1 contains three subdomains (N-terminal, α-helical, and parallel-F1-type-β-sheet core) and exhibits a complex vectoral topography that limits CFTR maturation (*22*, *25*) and prevents reversible folding in vitro. To examine its cotranslational folding pathway, FRET acceptor sites were chosen within 4 to 9 Å of the CFP fusion (Thr^{389}) (*26*) to report on the positioning of strands S3, S6, S7, and S8 in the β-sheet core (Fig. 1, B and C). Analysis of sequentially stalled polypeptides yielded a characteristic length-dependent rise and plateau in FRET for each acceptor site (Fig. 1D). This rise in FRET reports on acquisition of a native-like fold (*19*) and reflects the earliest biosynthetic stage at which the acceptor dye and its corresponding β-strand are optimally positioned within NBD1. Results show that S3, S6, S7, and S8 could therefore reach a native-like structure when the ribosome has synthesized residues 550, 624, 654, and 674, respectively (Fig. 1D), although actual folding intermediates will depend on relative folding kinetics and translation elongation rate.

Despite their proximity, S6 exhibited a more gradual rise in FRET and was optimally positioned at a later stage of synthesis than was S3 (Fig. 1D). Because the ribosome exit tunnel sequesters approximately 40 residues, optimal S6 positioning

[1]Department of Biochemistry and Molecular Biology, Oregon Health and Science University (OHSU), Portland, OR 97239, USA. [2]Department of Neuroscience and Cell Biology, University of Texas Medical Branch, Galveston, TX 77550-0620, USA. [3]Department of Biochemistry and Molecular Biology, University of Texas Medical Branch, Galveston, TX 77550-0620, USA. [4]Cystic Fibrosis Foundation Therapeutics, Bethesda, MD 20814, USA.
*Corresponding author. E-mail: skachw@ohsu.edu

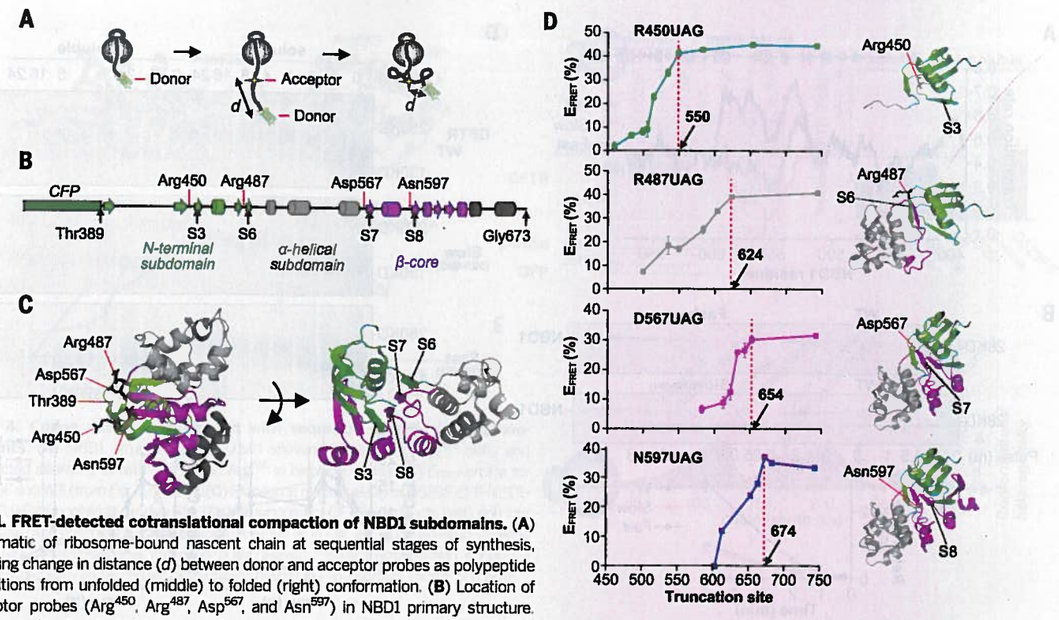

Fig. 1. FRET-detected cotranslational compaction of NBD1 subdomains. (**A**) Schematic of ribosome-bound nascent chain at sequential stages of synthesis, showing change in distance (*d*) between donor and acceptor probes as polypeptide transitions from unfolded (middle) to folded (right) conformation. (**B**) Location of acceptor probes (Arg^{450}, Arg^{487}, Asp^{567}, and Asn^{597}) in NBD1 primary structure. Helices and β-strands are drawn as cylinders and filled arrows, respectively. (**C**) Acceptor probe sites in NBD1 crystal structure [Protein Data Bank (PDB) 2BBO]. (**D**) FRET efficiency (E_{FRET}) plotted as a function of nascent chain length for indicated acceptor probe ($n \geq 3 \pm$ SEM or average of $n = 2$ replicates). Dotted line indicates synthetic stage needed to achieve maximal FRET. Shown on right is the minimal polypeptide outside the ribosome required to optimally position S3 (Arg^{450}), S6 (Arg^{487}), S7 (Asp^{567}), and S8 (Asn^{597}).

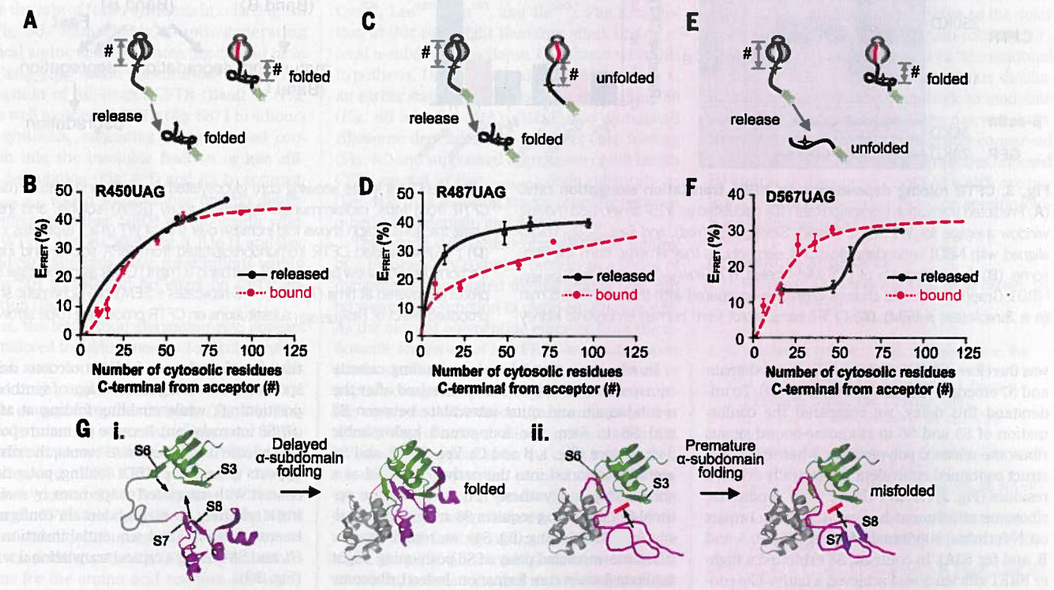

Fig. 2. Ribosome delays α-subdomain folding and facilitates β-sheet core formation. (**A**, **C**, and **E**) Illustration showing hypothetical folding outcomes of ribosome-bound and released polypeptides with equivalent cytosolically exposed residues. (**B**, **D**, and **F**) E_{FRET} obtained for ribosome released (black solid line) and ribosome-bound (red dotted line from Fig. 1D) polypeptides plotted against number of cytosolic residues (#) C-terminal to the acceptor site ($n \geq 3 \pm$ SEM or average of $n = 2$ replicates) located at residues 450, 487, 567, in (B), (D), and (F), respectively. (**G**) Illustration depicting (i) role of ribosome in delaying S6 and α-subdomain folding to facilitate S7 and S8 insertion and (ii) resultant NBD1 misfolding due to premature S6/α-subdomain folding in the absence of ribosome.